Environ Fluid Mech **20,** 987–1005 (2020). https://doi.org/10.1007/s10652-020-09736-8

Eulerian and Lagrangian time scales of the turbulence above staggered arrays of cubical obstacles

Annalisa Di Bernardino[1] • Paolo Monti[2] • Giovanni Leuzzi[2] • Giorgio Querzoli[3]

[1] Dipartimento di Fisica, Università di Roma "La Sapienza", Piazzale Aldo Moro 2, 00185 Roma, Italy.
[2] DICEA, Università di Roma "La Sapienza", Via Eudossiana 18, 00184 Roma, Italy.
[3] DICAAR, Università degli Studi di Cagliari, Via Marengo 2, 09123 Cagliari, Italy.

Corresponding author:
Paolo Monti, E-mail: paolo.monti@uniroma1.it; Tel.: +390644585045
ORCID: 0000-0001-5194-1351

Annalisa Di Bernardino. ORCID: 0000-0003-3765-2179
Giovanni Leuzzi. ORCID: 0000-0003-3929-6737
Giorgio Querzoli. ORCID: 0000-0003-3770-6034

Abstract

We present results from water-channel experiments on neutrally-stable turbulent flows over staggered arrays of cubical obstacles modelling idealised urban canopies. Attention is concentrated on the vertical profiles of the Eulerian (T^E) and Lagrangian (T^L) time scales of the turbulence above three canopies with different plan area fractions (λ_P =0.1, 0.25 and 0.4). The results show that both the streamwise and vertical components of T^L increase approximately linearly with height above the obstacles, supporting Raupach's linear law. The comparisons with the Lagrangian time scales over canyon-type canopies in the skimming flow and wake interference regimes show that the staggered configuration of cubical obstacles increases the streamwise T^L, while decreasing its vertical counterpart. A good agreement has also been found between the eddy viscosities (K_T) estimated by applying Taylor's theory and the classical first order closure relating the momentum flux to the velocity gradient. The results show that K_T obeys Prandtl's theory, particularly for $\lambda_P = 0.25$ and 0.4.

Keywords Building • Eddy diffusivity • Feature tracking • Raupach's law • Urban canopy • Water channel

1 Introduction

In a previous paper (Di Bernardino et al. [1], henceforth D17), we presented detailed Lagrangian and Eulerian statistics of the velocity field obtained from water-channel experiments mimicking the wind flow above idealised canyon-type canopies. Hereinafter, these will be referred to as “2D canopies”, while the staggered arrays of cubical obstacles we present here as “3D canopies”. One of the objectives of D17 was to quantify the Lagrangian (T^L) and the Eulerian (T^E) time scales of turbulence as well as to investigate their dependence on the aspect ratio of the canyon, $AR=W/H$, as the latter is the ratio of the street width (W) to the height (H) of the canopy. Knowledge of T^L remains of great importance, especially for applications in air pollution, e.g., Lagrangian models of turbulent dispersion [2]. These can be easily coupled with common Reynolds-averaged Navier–Stokes (RANS) models that do not compute T^L, which must be estimated from parametric laws generally applicable only over flat terrain.

T^L is defined as the time integral of the Lagrangian autocorrelation function of the fluctuating velocity, $\rho^L(\tau)$, viz.:

$$T^L = \int_0^\infty \rho^L d\tau \qquad (1)$$

and gives a rough measure of the time taken by the particle velocity to become decorrelated with its initial state (here τ is the time lag). Considerable efforts were made in the past to find suitable relationships between Eulerian and Lagrangian time scales of turbulence in view of the inherent difficulties in calculating ρ^L [3-4]. In fact, since Eulerian statistics can be easily determined from fixed-point measurements, the alternative estimate of T^L based on the work by Corrsin [5]:

$$T^L = \beta T^E \qquad (2)$$

is usually applied (e.g., [6-9]), where:

$$T^E = \int_0^\infty \rho^E d\tau \qquad (3)$$

is the Eulerian time scale of the turbulence. In Eq. (3), ρ^E is the Eulerian velocity autocorrelation function and $\beta = \gamma/i$ is a proportionality parameter, greater than unity, where i is the turbulence intensity and γ is a proportionality constant of order one. T^E gives a measure of the time needed by the turbulent velocity to become decorrelated with itself at a given location. Note that Corrsin's relation is strictly valid only for isotropic turbulence; in spite of that, it has been used in many cases studies.

Whilst measurements of T^E above urban canopies are commonly performed both in field campaigns [10] and in the laboratory [11], to our knowledge values of T^L above 3D urban canopies have not been published yet. Recently, Anfossi et al. [4] used a large-eddy simulation (LES) to estimate $\beta = T^L/T^E$ in an atmospheric boundary layer on flat terrain. They showed that β depends strongly on the flow stability and found that it generally falls into the interval 1–10 (note that those authors carried out values for β which must be considered as representative of the whole boundary layer). They also obtained a value for $\gamma = 0.41$ by combining all their LES runs for the three velocity components. A number of experimental, numerical and theoretical studies (see Fig. 1 in [8]) predicted for γ values around 0.4–0.6, while 0.35–0.8 was the γ range found by Hanna [3] by means of field experiments on flat terrain. To our knowledge, values for β for flows above staggered arrays of cubical obstacles have still not been carried out.

D17 observed that within the inertial layer (also known as to the constant flux layer, CFL) over flat terrain, both the streamwise and the vertical components of the

Lagrangian time scales, T_u^L and T_w^L, follow Raupach's [12] linear law, originally derived for one-dimensional turbulent flows:

$$\frac{T_w^L u_{*,ref}}{\delta} = \frac{k}{([\sigma_w/u_*]_{ref})^2}\frac{z}{\delta} \tag{4}$$

where k=0.41 is the von Karman constant, z the height, δ the boundary-layer height, u_* the friction velocity (i.e. the square root of the turbulent vertical flux of momentum), $u_{*,ref}$ and $\sigma_{w,ref}$ the reference values (i.e. averaged within the CFL) of u_* and of the standard deviation of the vertical velocity component, σ_w, respectively (these and other variables were computed as explained in Sect. 2 and 3). The expression for $T_u^L u_{*,ref}/\delta$ is identical to that of Eq. (4) but with $\sigma_{u,ref}$ in place of $\sigma_{w,ref}$, where the former is the reference value of the standard deviation of the streamwise velocity component.

Equation (4) was obtained by matching the expressions of the linear growth with height of the eddy diffusivity of momentum based on Prandtl's mixing-length theory, $K_T = ku_*z$, and the far-field eddy diffusivity, $K_T = \sigma_w^2 T_w^L$ [13]. D17 found a reasonable agreement between T_u^L, T_w^L and Eq. (4) in 2D canopy flows, except for T_u^L when AR=2 (wake-interference regime, see below), which differed considerably from T_w^L for $z/H \lesssim 2$, i.e. within the roughness sublayer (RSL) and the lower part of the CFL. The former is the portion of boundary layer immediately above the canopy where the flow is non-homogenous and strongly influenced by the roughness elements constituting the canopy [14]. In that case, H can be used as a reliable scale variable in place of δ and the distance from the bottom on the right-hand term of the equation is lowered by the displacement height, d, i.e., the effective height of the ground due to the vertical flow displacement through the canopy. Note that Raupach's law is a simple expression whose terms can be obtained from routine one-point measurements.

Owing to the growing interest of the scientific community in predicting wind flow and pollutant dispersion in more common, three-dimensional urban canopies – see recent experimental [15-19] and numerical [20-22] works on that subject –, we used the same water-channel apparatus of D17 to investigate the turbulent flow above staggered arrays of cubical obstacles. Three experimental arrangements were considered for the analysis as a function of the plan area fraction, $\lambda_p = A_p/A_T$, i.e., the ratio of the plan area of roughness elements to the total surface area. In particular, the first arrangement, $\lambda_p = 0.1$, refers to the isolated-flow regime ($\lambda_p < 0.13$), where the interaction between individual building wakes is weak; the second, $\lambda_p = 0.25$, corresponds to the wake-interference regime ($0.13 < \lambda_p < 0.35$), in which the spacing between buildings is close enough that for the wakes to strengthen each other; while the third, $\lambda_p = 0.4$, belongs to the skimming flow regime, i.e. when the obstacles are so packed that the outer flow skips over their tops ($\lambda_p > 0.35$) (see e.g. [23]). Whilst the wake-interference regime has been widely studied in the literature, in particular the case $\lambda_p = 0.25$, which is practically assumed as an archetype for 3D building arrays ([24-27], among others), less attention has been paid to the other two regimes (see, e.g., [28-30]), although they belong to the range of plan area fractions typically found in real cities [31].

After a brief description of the experimental setup and data analysis (Sect. 2), the paper reports Lagrangian and Eulerian statistics of the flow (Sect. 3), also paying attention to differences or similarities with the 2D case. Here, we present an analysis of the vertical profiles of both the Eulerian and Lagrangian time scales of the turbulence and of their ratio β obtained for the three λ_p. In addition, information is also given on the turbulent diffusivity of momentum. The final remarks are presented in Sect. 4.

2 Experimental Setup and Data Analysis

2.1 Water channel and acquisition facility

The experiments were conducted in the recirculating water channel of the Hydraulic Laboratory of the University of Rome – La Sapienza, Italy [32]. The channel (7.4 m long) has a rectangular cross section 0.35 m high and 0.25 m wide. To observe the flow visually, the lateral sides of the tank are made of transparent glass. The flume is fed by a constant head reservoir. A neutral boundary layer is recreated increasing the roughness of the channel bottom via randomly distributed pebbles with average diameter ≈5 mm. The water depth and the free-stream velocity are 0.16 m and U=0.34 m s^{-1}, respectively.

The test section is positioned nearly 5 m downstream of the inlet, where the boundary layer is fully developed. Each array of obstacles is designed by means of uniform, sharp-edged cubes with height H=15 mm glued onto the channel bottom in a staggered pattern (Fig. 1). Details of the three arrays are given in Table 1 and Fig. 2.

Table 1 Geometrical characteristics of the three cubic arrays

	$\lambda_P = 0.1$	$\lambda_P = 0.25$	$\lambda_P = 0.4$
Element distance (mm, see Fig. 2)	32	15	9
Unit size (mm^2)	47	30	24

In order to analyse both the Eulerian and Lagrangian properties of the flow, two different acquisition setups were used. In particular, the Eulerian velocity field was measured on a rectangular area lying in the vertical x–z plane (0.11 m long and 0.055 m high) passing through the centre of the channel (see green lines in Fig. 2). The measurement area was illuminated by a thin light sheet (≈2 mm thick) from a 5 W green laser (CNI©, model MGL-W-532A) equipped with a Powell lens with a 12° fan angle. A thin Plexiglas slab (250 mm spanwise by 300 mm streamwise dimension) with raised edges was carefully aligned with the free water surface in order to avoid perturbations of the light sheet. The water was seeded with Titanium dioxide particles, 20 μm in diameter, uniformly dispersed in the working fluid (about 3,500 particles were recognized over each frame). The particles were assumed as being transported passively by the flow since the estimated sedimentation velocity was as small as 0.6 mm s^{-1}. Each experiment consisted of a set of N=10,000 images acquired by means of a high-speed video camera (Mikrotron, EoSens 1362, set at 250 Hz, 1280x1024 pixels in resolution, with a Nikkor 105mm, f 2.5, lens, and a 12mm extension tube).

To reconstruct the particle trajectories needed to determine the Lagrangian velocities, a second set of experiments was run in the same flow conditions but changing the acquisition setup so that the longest possible trajectories could be acquired. To this aim, the framed area was enlarged to 0.30x0.15 m^2 and the flow was illuminated by a thicker light sheet (0.02 m in depth, yellow areas in Fig. 2) generated by a 1000 W, white halogen lamp with the optics of a slide projector and a diaphragm consisting of an opaque surface mounted on a slide frame, with a thin vertical slit at its centre. The increased thickness of the light sheet ensures that only a negligible fraction of the trajectories is truncated because of spanwise displacement. During each experiment nearly 100,000 images were acquired at a 500 Hz frame rate with the same high-speed camera and resolution as above, and a Zeiss 50mm, f 1.4 lens. The seeding density was decreased in order to have a low number of particles at the same time in the illuminated volumes (about 600). As a result, the mean particle distance on the acquired images was about 50 pixels, i.e. much higher than the typical particle displacement during the time interval between frames (as low as 1 or 2 pixels because of the increased frame rate). In this way, the ambiguity during the tracking procedure was minimised.

2.2 Velocity measurements

Velocity fields were obtained by using a feature tracking technique, which is a modified version of the KLT tracker [33]. It recognises particle trajectories and deduces velocities from particle displacements between successive frames. The first step is selecting points of the images that can be successfully tracked between frames, the so-called features. In our application, they correspond to the seeding particles. Secondly, the features are tracked over multiple frames following a strategy that minimises possible errors in the trajectory recognition. The feature selection is based on a criterion which is optimal from the point of view of the tracking algorithm. The displacement of the features between successive frames is found under the assumption of the invariance of particle images during their motion [34]: $DI(\boldsymbol{x},t)/Dt = 0$, where $D\bullet/Dt$ indicates the Lagrangian derivative and $I(\boldsymbol{x},t)$ the light intensity on the image at time t and position $\boldsymbol{x}$. Due to the presence of noise in the acquired images, we cannot impose the above invariance at each single pixel of the image. More robustly, we impose the minimisation of the following residue over an interrogation window, W (11×11 pixels in our experiments) [35]:

$$\varepsilon = \int_W \left(\frac{DI(\boldsymbol{x},t)}{Dt}\right)^2 dW = \int_W \left(\frac{\partial I(\boldsymbol{x},t)}{\partial t} + \nabla I(\boldsymbol{x},t)\boldsymbol{u}\right)^2 dW \tag{5}$$

where $\boldsymbol{u}$ indicates the particle velocity, which is directly related to the displacement, $\boldsymbol{d} = \boldsymbol{u}\Delta t$, by means of the time interval between frames, Δt. In order for ε to be a minimum, the derivatives of the residue with respect to the velocity components must be set to zero, thus yielding a set of two equations where the two velocity components are the unknowns:

$$G\boldsymbol{u} = \boldsymbol{e} \tag{6}$$

where:

$$G = \int_W \begin{bmatrix} \left(\frac{\partial I}{\partial x}\right)^2 & \left(\frac{\partial I}{\partial x}\frac{\partial I}{\partial y}\right) \\ \left(\frac{\partial I}{\partial x}\frac{\partial I}{\partial y}\right) & \left(\frac{\partial I}{\partial y}\right)^2 \end{bmatrix} dW \tag{7}$$

and

$$\boldsymbol{e} = \int_W \frac{\partial I}{\partial t}\begin{bmatrix} \frac{\partial I}{\partial x} \\ \frac{\partial I}{\partial y} \end{bmatrix} dW \tag{8}$$

The above set of linear equations can be solved reliably provided that both the eigenvalues of G, computed over the interrogation window W, are about of the same order of magnitude and not too small compared to the image noise level. In practice, to select the good features to track [36], we use a threshold criterion on the second (minimum) eigenvalue: firstly, we compute the eigenvalues of G for every possible window over the image; secondly, we look for local maxima of the minimum eigenvalue and, thirdly, we accept the centre of a window, W, as a "good feature to track" (a valid particle location) provided that: *i)* the second eigenvalue exceeds an assigned threshold value and *ii*) there are no other local maxima with higher second eigenvalues within an assigned radius, r_{min} (chosen to be larger than the typical particle size, 5 pixels for our experiments). As a matter of fact, high eigenvalues are found in the regions of the image where spatial gradients of the light intensity are large and local maxima correspond to the bright spots left by the seeding particles. The second condition avoids multiple recognitions of the same particle.

The particle recognition and tracking procedures described above were combined to recognise particle trajectories. At each time instant:

i) The next location of the presently tracked particle was predicted using the velocity evaluation algorithm described above. The new particle location was considered valid and added to the corresponding trajectory provided the minimum eigenvalue on the present image exceeded a given threshold value.

ii) After the existing trajectories were continued (step *i*), the present image was searched for new features to track using the algorithm described above. Again, in order to avoid multiple recognitions of the same particle, a new feature was accepted only if the minimum distance from other validated features exceeded r_{min}.

In order to minimise possible trajectory recognition errors and consequent spurious velocity samples, a trajectory was assumed valid only if it consisted of at least three points [37].

Though the algorithm was the same, Lagrangian and/or Eulerian data were saved separately depending on the aim of the experiment.

The Eulerian dataset consisted of the set of sparse instantaneous velocity samples obtained from particle displacements of tracked particles at each time step. The Lagrangian dataset was obtained by storing the succession of positions forming a trajectory each time a particle could no longer be tracked.

2.3 Eulerian statistics

In order to compute the Eulerian statistics, a Gaussian interpolation algorithm was applied to the scattered data (about 3500 velocity samples per frame, on average) so as to obtain the instantaneous velocity fields on a regular grid. The results thus obtained have a spatial resolution of 1 mm and a temporal resolution of 1/250 s. Additional experiments were also conducted framing the free surface to evaluate the free-stream velocity and the turbulent boundary-layer depth.

The statistics of the Eulerian velocity fields were obtained by time averaging over the *N* time instants. The mean velocity components $\overline{u}(m,n)$ and $\overline{w}(m,n)$, the variances $\sigma_u^2(m,n) = \overline{u'^2}(m,n)$ and $\sigma_w^2(m,n) = \overline{w'^2}(m,n)$ as well as the vertical momentum flux $\overline{u'w'}(m,n)$ have been calculated at each node (m,n) of the 110 (along x) x 55 (along z) grid (the prime is the fluctuation around the mean). Uncertainty in the evaluation of the statistics presented in the following has been estimated from their standard deviation computed over each experiment [38] and is reported in the captions of the corresponding figures.

The Eulerian time scales for the velocity component along the *j*-th axis is calculated as:

$$T_j^E = \int_0^\infty \rho_j^E(\tau)d\tau = \int_0^\infty \frac{\overline{v_j'(t)v_j'(t+\tau)}}{\sigma_j^2}d\tau \qquad (9)$$

where $\rho_j^E(\tau)$ is the Eulerian autocorrelation function of the *j*-th velocity component, v_j.

2.4 Lagrangian statistics

The Lagrangian time scales were calculated from the set of particle trajectories longer than 350 instants (corresponding to 0.7 s) detected during the image-processing procedure. The results presented below show that such a minimum length is adequately larger than the turbulence time scale for all the three configurations analysed. The total number of trajectories exceeding the requested length during each experiment is listed in Table 2. As an example of particle trajectories, Fig. 3 shows some of the particles tracked for more than 350 instants ($\lambda_p = 0.25$).

Table 2 Number of trajectories exceeding the minimum length (corresponding to 350 instants) for the three experiments

	$\lambda_p = 0.1$	$\lambda_p = 0.25$	$\lambda_p = 0.4$
Number of trajectories	129,801	161,259	135,950

Let us assume that the tracking of the k-th particle starts at reference time $t_0^{(k)}$ and reference position $\boldsymbol{x}_0^{(k)}$. We indicate its position and velocity at a generic time by $\boldsymbol{X}^{(k)}\left(\boldsymbol{x}_0^{(k)}, t_0^{(k)}, t\right)$ and $\boldsymbol{U}^{(k)}\left(\boldsymbol{x}_0^{(k)}, t_0^{(k)}, t\right)$, respectively (letters in capital refer to Lagrangian properties, while bold indicates vector quantities). Furthermore, provided the phenomenon is statistically steady in a Eulerian sense, averages are independent of the reference time $t_0^{(k)}$. However, they still depend on the time lag, $\tau = t - t_0^{(k)}$, and reference position $\boldsymbol{x}_0^{(k)}$. Consequently, following Monin and Yaglom [39] the Lagrangian mean velocity can be written as:

$$\langle \boldsymbol{U} \rangle (\boldsymbol{x}_0, \tau) = \frac{1}{M_{\boldsymbol{x}_0}} \sum_{k|_{\boldsymbol{x}_0}} \boldsymbol{U}^{(k)}(\boldsymbol{x}_0, \tau) \tag{10}$$

where the summation refers to the $M_{\boldsymbol{x}_0}$ trajectories starting from $\boldsymbol{x}_0$. Similarly, the standard deviation of the j-th component of the velocity is computed as:

$$\sigma_j^L(x_0,\tau) = \sqrt{\frac{1}{M_{x_0}} \sum_{k|_{x_0}} \left[U_j^{(k)}(x_0,\tau) - \langle U_j\rangle(x_0,\tau)\right]^2} \qquad (11)$$

while the auto-correlation coefficient is expressed as:

$$\rho_j^L(x_0,\tau) = \frac{1}{M_{x_0}} \frac{\sum_{k|_{x_0}} \left\{\left[U_j^{(k)}(x_0,\tau) - \langle U_j\rangle(x_0,\tau)\right]\left[U_j^{(k)}(x_0,0) - \langle U_j\rangle(x_0,0)\right]\right\}}{\sigma_j^L(x_0,\tau)\sigma_j^L(x_0,0)} \qquad (12)$$

The Lagrangian time scale of the *j*-th velocity component, T_j^L, is evaluated as the integral of the corresponding Lagrangian autocorrelation function, viz. [39]:

$$T_j^L(x_0) = \int_0^\infty \rho_j^L(x_0,\tau)d\tau \qquad (13)$$

Other methods of calculation of the Lagrangian autocorrelation function in homogeneous and inhomogeneous turbulent flows are reported in [40] and [41].

It should be pointed out that we track only particles remaining in the 20mm deep light sheet at least 0.7 s. Therefore, in principle, Lagrangian statistics could be affected by a bias due to this selective sampling. However, the measuring volume is located above the canopy, where crossflow motions are typically non-dominant, and we observed that most of the trajectories crossed the whole measuring field without leaving from the lateral boundaries.

3 Results and Discussion

Details regarding the characteristics of the approaching flow upwind of the arrays (e.g. vertical profiles of mean velocity, turbulence properties and integral time scales) can be found in D17 and are not repeated here. Given the flow three-dimensionality, an average of the variables over an adequately large number of individual sections belonging to different vertical planes parallel to the streamwise direction would be necessary to obtain representative spatially-averaged properties of the flow. However, to avoid very time-consuming experiments, it was decided to consider only the vertical section passing through the centre of the obstacles (see green lines in Fig. 2). With regard to the previous issue, [42] showed that for a regular array of staggered cubical obstacles with $\lambda_p = 0.25$ no significant errors occur by considering only measurement points belonging to the vertical plane passing through the middle section of the obstacles. Such a simplification may be inappropriate for other geometrical arrangements [42], even though the regular dispositions of the cubes considered in our experiments might do not involve appreciable errors, particularly for $\lambda_p = 0.4$.

The vertical profiles of the Eulerian variables were estimated by adopting the canopy approach (e.g., [43]), namely by horizontally averaging the time averaged statistics over a region including one building top and the contiguous canyon. In doing so, the results can be assumed as representative of the repeating unit constituting the canopy, keeping in mind the limitation mentioned above.

3.1 Mean Velocity and Reynolds Stresses

Figure 4 shows the vertical profiles of the normalised streamwise velocity component (Fig. 4a), Reynolds shear stress (Fig. 4b) and standard deviation of the horizontal (σ_u) and vertical (σ_w) velocity components (Fig. 4c) for the three arrays. For $\lambda_p = 0.25$ (wake-interference regime), the profiles are quantitatively similar to those reported by other authors (see e.g. [42]). The Reynolds shear stress varies up to $z \approx 2H$ (i.e. the RSL depth), then it is nearly independent of z up to $z/H \approx 3.2H$, which can be considered as the upper limit of the CFL (Fig. 4b). While the $\lambda_p = 0.4$ case (skimming flow) behaves similarly to $\lambda_p = 0.25$, for $\lambda_p = 0.1$ (isolated regime) the RSL is considerably deeper and the CFL forms at $z \approx 2.75H$. This agrees with other observations conducted in the laboratory [44] and in the real field [45].

We assume as reference friction velocity, u_{*ref}, the average of the local friction velocity, $u_* = \sqrt{-\overline{u'w'}}$, calculated within the CFL, i.e. $u_{*ref} = 0.019$, 0.0169 and

0.0173 ms^{-1} for $\lambda_p = 0.1$, 0.25 and 0.4, respectively. The resulting roughness Reynolds numbers based on the obstacle height, $Re_\tau = u_{*,ref}H/\nu$, are larger than 250 ($\nu = 10^{-6}$ m^{2}s^{-1} is the kinematic viscosity of water), i.e. greater than the critical value, $Re_c = 70$, required to ensure the attainment of a fully-rough-wall regime [46-47].

Note that $\sigma_w/u_{*,ref}$ and $\sigma_u/u_{*,ref}$ do not change appreciably with height in the whole z/H range analysed, with the $\lambda_p = 0.1$ case showing slightly larger values, in agreement with the direct numerical simulations of [48]. The similarity found between $\lambda_p = 0.25$ and 0.4 is not surprising since in terms of classical roughness terminology the former can be considered as near the so-called 'd-type' roughness – the same one to which the latter belongs – where the cavities sustain stable recirculating vortices that isolate the upper flow from the inner one. In contrast, lower λ_p are typical of 'k-type' roughness, where the distribution of the roughness elements is sparse and vortex shedding between the elements characterises the flow (see [49-51] and [20] for more discussion on this subject).

Recent wind-tunnel results by [17] on the effect of building packing density on the drag force over aligned arrays of cubes show that the shear stress increases with increasing packing density up to $\lambda_p = 0.25$. The larger Reynolds shear stress we found for $\lambda_p = 0.1$ compared to $\lambda_p = 0.25$ and 0.4 therefore goes against [17]. One possible reason for this disagreement could be the different geometry of the cube arrays used, i.e. aligned for [17] and staggered in our case, where the latter is known to be characterised by higher stresses than the aligned one [42]. Therefore, it is reasonable that the maximum stress measured in our experiments and by [17] may not take place at the same packing density. On the other hand, direct numerical simulations conducted by [48] for staggered arrays of cubical obstacles (like those considered in our experiments) showed that the total shear stress peaks for $\lambda_p \approx 0.13$, i.e. not far from our $\lambda_p = 0.1$. In particular, [48] found $u_\tau/U_b \approx 0.12$ and ≈0.11 for $\lambda_p = 0.11$ and 0.25, respectively (here u_τ and U_b are the total shear stress and the bulk velocity, where the latter corresponds with the velocity averaged over the whole depth of the investigated domain). These values are in line with $u_*/U_b \approx 0.095$ and ≈0.085 calculated from our experiments for $\lambda_p = 0.1$ and 0.25, respectively (note that u_τ is nearly 15% larger than u_* [48]). However, we must always bear in mind that we considered only the vertical plane passing through the cube centre to measure the velocity field (see discussion at the beginning of the present section).

3.2 Eulerian Integral Time and Spatial Scales

The Eulerian time scales for the streamwise and the vertical velocity components, T_u^E and T_w^E, respectively, are estimated using Eq. (13) considering the time at which the autocorrelation decreases to $1/e$ (here, e is the Euler number). This is a very common procedure for the extraction of integral time scales since the mathematical form of the autocorrelation is generally a decaying exponential [52]. The characteristic time based on the mean building height, $H/u_{*,ref}$, is used to normalise T_u^E and T_w^E.

Analysis of Fig. 5a suggests that: (*i*) overall, the three non-dimensional T_u^E (continuous lines with symbols) increase approximately linearly with height within the RSL, then they remain nearly constant in the overlying CFL; (ii) T_u^E does not change much with λ_p, although larger T_u^E occur for $\lambda_p = 0.1$ at the top of the cavity; (iii) T_w^E increases slightly with height irrespective of λ_p; the two T_w^E for $\lambda_p = 0.25$ and 0.4 share nearly the same profile, while T_w^E for $\lambda_p = 0.1$ (isolated flow) is around twice those calculated for the other two λ_p.

The strict similarity between $\lambda_p = 0.25$ and 0.4 can be further supported by analysing the integral spatial scales of the streamwise velocity component:

$$L_{u,x} = \int_0^\infty R_u \, dx \quad ; \quad L_{u,z} = \int_0^\infty R_u \, dz \qquad (14)$$

where

$$R_u(\boldsymbol{x}_0,\boldsymbol{r}) = \frac{\overline{u'(\boldsymbol{x}_0)u'(\boldsymbol{x}_0+\boldsymbol{r})}}{\sigma_u(\boldsymbol{x}_0)\sigma_u(\boldsymbol{x}_0+\boldsymbol{r})} \qquad (15)$$

is the spatial autocorrelation function of the u-component and $\boldsymbol{r}$ is the displacement relative to the reference location $\boldsymbol{x}_0$. Spatial scales represent a measure of the distance along which the velocities are correlated and, in general, they give useful insight into the flow structure [44][53-55]. As for the integral time scales, we obtain the vertical profiles of $L_{u,x}$ and $L_{u,z}$ (i.e., the spatial autocorrelations of the u-component along x and z, respectively) moving $\boldsymbol{x}_0$ along the vertical axis passing through the centre of the cavity and evaluating the distance where the autocorrelation decreases to $1/e$ (due to technical limitations, the case $\lambda_p = 0.1$ was not suitable for spatial autocorrelation estimate and, therefore, no spatial scales are presented here for that plan area fraction). $L_{u,x}$ and $L_{u,z}$ for both cases grow within the RSL and reach an asymptotic value ($L_{u,x} \approx 2.7H$, $L_{u,z} \approx 0.9H$) in the CFL (Fig. 5b), and show a reasonable agreement with those found by [55] for a staggered cube array with $\lambda_p = 0.25$. Note that the position of the vertical profile considered by [55] (profile "P2", just ahead of the cube) differs from that used in the present work. However, while $L_{u,x}$ and $L_{u,z}$ within the canopy depend substantially on the profile location, above the cubes these differences are expected to be smaller, especially in the CFL [55]. Figure 5b also shows $L_{u,x}$ (blue line) and $L_{u,z}$ (black line) estimated by [17] on flat terrain (here, $L_{u,x}$ and $L_{u,z}$ have been rescaled with H). The diminishing effect of the canopy is evident on both the scales within the RSL (nearly a factor of 2 and 3 at z=1.15H for $L_{u,x}$ and $L_{u,z}$, respectively).

The resemblance between the skimming flow and wake-interference regime discernible from Eulerian scale analysis contrasts with was observed by D17 for 2D street canyons, where the dissimilarities between those two regimes were noticeable. For ease of comparison, Fig. 5a shows T_u^E and T_w^E estimated by D17 for aspect ratios AR=1 (dashed lines) and 2 (dotted lines). We see that for AR=1 (corresponding to $\lambda_p = 0.5$, i.e. skimming flow) T_u^E and T_w^E are in line with those estimated for $\lambda_p = 0.25$ and 0.4, although T_u^E for AR=1 is lower for z>2H. In contrast, larger T_u^E and T_w^E occur for AR=2 (corresponding to $\lambda_p = 0.33$, i.e., wake-interference regime) compared to their 3D counterparts. The origin of these dissimilarities could be related to the profound differences existing between skimming flow and wake-interference regime for 2D street canyons (see e.g., [56-59]), also in terms of different sizes of the coherent structures characterising those two flows [1] (see [55] for a comprehensive discussion on the subject).

3.3 Lagrangian Integral Time Scales

Two-dimensional fields of ρ_u^L and ρ_w^L can be determined using Eq. (12) and considering all the trajectories starting in the proximity of each node of the Eulerian grid. However, given the quasi-horizontal homogeneity of the flow above the canopy, ρ_u^L and ρ_w^L are calculated following all the trajectories that start within a 1 mm thick layer, extended horizontally over the whole domain, passing through the nodes of the Eulerian grid. We consider the trajectories only once in the calculation of the statistics avoiding their multiple use in different layers. The size of $\boldsymbol{x_0}$ along the vertical is 1 mm, i.e., about 42 pixels. Tolerance is of the order of the pixel. Examples of ρ_u^L and ρ_w^L calculated at $z/H = 1.83$ for $\lambda_p = 0.25$ are depicted in Fig. 6. These autocorrelations were obtained considering 1340 trajectories, whose length is such as to ensure the autocorrelations to fall to 1/*e*. Both the autocorrelations can be approximated by decaying exponentials (R^2=0.93–0.99). The resulting T_u^L and T_w^L are determined using Eq. (13) by considering the time lag when the autocorrelations decrease to 1/*e*. As for the Eulerian scales, H/u_{*ref} is used to normalise T_u^L and T_w^L (Fig. 7).

Overall, the 3D canopy tends to decrease the scale of the vertical velocity component while increasing the scale of the horizontal component as compared to the 2D case [1]. The three T_u^L (solid symbols) show a linear growth with height up to $z \approx 3.5H$ (R^2 equal to 0.99, 0.85 and 0.97 for $\lambda_p = 0.1$, 0.25 and 0.4, respectively, see the linear fits represented by the dashed lines in the figure), and a quasi-constant trend above. The slopes of the linear fits are around 0.24 for $\lambda_p = 0.25$ and 0.4. Owing to the large amount of data scatter occurring for $\lambda_p = 0.25$ (probably due to unwanted effects associated with light reflection at the cube tops), a certain degree of caution is required when interpreting the results for this cube arrangement. On the other hand, $T_u^L u_{*ref}/H$ grows faster when $\lambda_p = 0.1$ (now the slope is around 0.4) and reaches a maximum nearly 20% larger than that observed for the other two λ_p. However, $T_u^L u_{*,ref}/H \approx 1$ above $3.5H$ for all the three cases.

With regard to T_W^L, it increases linearly with height up to $z \approx 5H$ (R^2>0.96) irrespective of λ_p and it is always lower than T_u^L. For $\lambda_p = 0.25$ and 0.4, $T_u^L \approx (2-3)T_W^L$ in the whole boundary layer analysed, including the region near the top of the obstacles. The latter is a significant difference with the results of D17 for the 2D skimming flow (*AR*=1), where $T_u^L \approx T_W^L$ up to *z*=3*H* (red and blue lines in Fig. 7c). These differences can be of importance in dispersion of pollutants modelling.

It is current practice in plant-canopy studies to derive T_W^L through Eq. (4) [60,61], while, as far as we are aware, Eq. (4) has never been used for staggered arrays of cubical obstacles (and in general for 3D urban canopies). It is therefore worthwhile testing the Eq. (4) capability to predict T_W^L for our three geometrical arrangements. As mentioned in the introduction, in the presence of a canopy Eq. (4) can be rewritten as (see e.g. [60]):

$$\frac{T_W^L u_{*ref}}{H} = \frac{k}{([\sigma_w/u_*]_{ref})^2}\,\frac{z-d}{H} \qquad (16)$$

where the displacement heights *d*=0.56*H*, 0.78*H* and 0.93*H* for $\lambda_p = 0.1$, 0.25 and 0.4, respectively, have been calculated by means of the empirical law by [62]. Fig. 7 shows that T_W^L calculated through Eq. (16) (continuous line) are similar in value to experimental values (open diamonds) close to the cube tops in all three cases, especially for $\lambda_p = 0.4$, when they differ nearly 20% at *z*=3*H*. The fact that Eq. (16)

approximates reasonably the vertical profile of T_w^L also for staggered arrays of cubical obstacles could be of some interest for the prediction of flow and pollutant dispersion over urban areas.

3.4 Lagrangian to Eulerian Time Scales Ratio

The vertical profiles of the Lagrangian to Eulerian integral scale ratios (β) are depicted in Fig. 8. As mentioned in the introduction, the definition of β is strictly valid only for isotropic turbulence; values of β for flows above staggered arrays of cubic obstacles have still not been carried out. The ratio of the streamwise component, $\beta_u = T_u^L/T_u^E$ (solid diamonds), is always lower than the vertical one, $\beta_w = T_w^L/T_w^E$ (open diamonds). This agrees with the LES results of [4], who found $\beta_u = 5.09$ and $\beta_w = 10.24$ (these values averages over the whole boundary-layer depth in the case of flat terrain) and with the 2D canopy flow experiments by D17. Despite some β_u oscillations for $\lambda_p = 0.25$ (this reflects the T_u^L data scatter above the rooftops), Fig. 8 suggests that both β_u and β_w grow with height at least of a factor of two in the analysed layer. They are always larger than unity, as generally expected in the presence of a mean flow [3].

Owing to the inherent difficulties of $\beta = T^L/T^E$ measurements in the real field, it is worthwhile to compare Corrsin's expression $\beta = \gamma/i$ (whose determination is certainly simpler, see Sect. 1) against our experimental results. The agreement between T_u^L/T_u^E and γ_u/i_u (continuous line, $i_u = \sigma_u/\bar{u}$ is the turbulence intensity in the *x*-direction) is poor for $\lambda_p = 0.25$ up to $z \approx 3H$ regardless of the value chosen for γ_u (again, this might be related to the T_u^L scatter mentioned above). In contrast, their agreement is reasonable for $\lambda_p = 0.1$ and 0.4 once setting $\gamma_u = 0.5$. This latter value is in line with those found for flat terrain by [4] and in many other studies as summarised in [8], although γ_u is expected to depend on the surface characteristics [63]. For the 2D street-canyon geometry D17 found $\gamma_u = 0.35$ for *AR*=1 and 2.

Regarding the vertical direction, $\gamma_w/i_w = 0.5/i_w$ (dashed line, where $i_w = \sigma_w/\bar{u}$ is the turbulence intensity in the *z*-direction) is in satisfactory agreement with $T^L_{w'}/T^E_{w'}$ (open diamonds) for $\lambda_p = 0.25$ and 0.4 (here $i_{w'} = \sigma_{w'}/\overline{u}$) but not for $\lambda_p = 0.1$, which is best approximated if $\gamma_{w'} = 0.35$ (the reader must always recall that the results for $\lambda_p = 0.1$ have to be considered with a certain degree of caution because the analysis carried out on a single section passing through the centerline section of the buildings may not be representative of a complex flow such as the one established for $\lambda_p = 0.1$ due to the distance between the buildings themselves). However, all the values found for γ_u and γ_w fall well into the range generally found in the literature (0.4–0.8) in the case of flows with small turbulent intensity.

We can therefore say that γ/i is a reasonable approximation of T^L/T^E also above staggered arrays of cubical obstacles regardless of the velocity component.

3.5 Turbulent Diffusivity

We conclude the analysis by presenting in Fig. 9 comparisons of the vertical profiles of two estimations of the turbulent diffusivity, K_T. The first is based on the first-order closure for the momentum flux, $K_{T,fo} = -\overline{u'w'}\, d\overline{u}/dz$ (blue circles), while the second relies on Taylor's theory, $K_{T,T} = \sigma_{w'}^2 T_{w'}^L$ (red crosses). Even though the former frequently fails in the presence of large eddies, it is commonly adopted in computational fluid dynamics. The agreement between the two is reasonable both within and above the RSL, with the exception of the $\lambda_p = 0.25$ case, where differences occur particularly close to the roof top (as mentioned above, this could be due to anomaly caused by illumination problems during the acquisition).

$K_{T,fo}$ and $K_{T,T}$ grow roughly linearly with height and are not far from the eddy diffusivity based on Prandtl's mixing-length theory, $K_{T,P} = k u_{*ref}(z - d)$ (solid line), to be assumed valid in principle only within the CFL, where local equilibrium between momentum flux and wind gradient holds. We would have expected a better agreement of $K_{T,fo}$ and $K_{T,T}$ with $K_{T,P}$ in the CFL rather than in the RSL since only in the former region the logarithmic law is valid (see for example discussion in [61]). It should however be noted that the slopes of all the three formulations are very sensitive to values set for the von Karman constant and the reference friction velocity. For instance, by setting *k*=0.37 (a value within the range typically reported in the literature [64]) in place of 0.41 the slopes of the three formulations match in the CFL. It can be concluded that it stands to reason that Prandtl's mixing-length theory can be assumed as a realistic approximation for the eddy diffusivity of momentum above 3D canopies, at least for the skimming flow and the wake-interference regimes.

4 Concluding remarks

Results from water-channel experiments on the turbulent flow above staggered arrays of cubical obstacles mimicking idealised urban canopies for three different plan area fractions ($\lambda_p = 0.1$, 0.25 and 0.4) were presented. All the experiments refer to neutral conditions. The attention is focussed on the Lagrangian and Eulerian time scales of the turbulence and on the eddy diffusivity of momentum. The main findings include the following:

i) Although in the literature regular obstacle arrays with $\lambda_p = 0.25$ and 0.4 are considered belonging to different flow regimes (wake interference and skimming flow, respectively), no substantial differences among most of the measured quantities for the two cases appear above the top of the obstacles (the only noticeable difference regards the turbulent viscosities calculated via Taylor's theory, see point iii of this list). This is understandable in that $\lambda_p = 0.25$ and 0.4 can be both classified as d-type roughness, where exchanges of mass and momentum between inner and outer flow are small. In contrast, the case $\lambda_p = 0.1$ (isolated flow, classified as k-type roughness) behaves differently from the other two.

ii) Both the streamwise, T_u^L, and the vertical, T_w^L, components of the Lagrangian time scale of the turbulence increase approximately linearly with height up to $z \approx 3.5H$ and $5H$, respectively, therefore including the roughness sublayer and part of the constant flux layer that forms above the canopy. Especially, to the best of our knowledge, this is the first time that experimental evidence on the agreement between T_w^L and Raupach's [16] law has been presented for 3D arrays of cubical obstacles. $\beta_w = T_w^L/T_w^E$ and $\gamma_w \bar{u}/\sigma_w$ agree reasonably well in all the three geometries, while the agreement between $\beta_u = T_u^L/T_u^E$ and $\gamma_u \bar{u}/\sigma_u$ is poor for $\lambda_p = 0.25$, probably because of scatter in the T_u^L data within the investigated boundary layer.

iii) The turbulent viscosity (K_T) estimated by applying the first order closure shows a linear growth with height, in accordance with Prandtl's theory, within and above the RSL for all the three λ_p. This suggests that the latter, simple form of K_T might be used with a certain degree of reliability, at least for $\lambda_p = 0.25$ and 0.4. A reasonable agreement between Prandtl's theory and K_T calculated applying Taylor's theory also holds, although for $\lambda_p = 0.25$ the latter determination of K_T differs substantially from those obtained by applying the first order closure and Prandtl's theory.

Acknowledgements This research was supported by the RG11715C7D43B2B6 fund from the University of Rome "La Sapienza". The assistance of Manuel Mastrangelo and Cristina Grossi (Master degree students at the University of Rome "La Sapienza") to the measurements was greatly appreciated.

References

1. Di Bernardino A, Monti P, Leuzzi G, Querzoli G (2017) Water-channel estimation of Eulerian and Lagrangian time scales of the turbulence in idealized two-dimensional urban canopies. Bound-Layer Meteorol 165:251–276
2. Thomson DJ (1987) Criteria for the selection of stochastic models of particle trajectories in turbulent flows. J Fluid Mech 180:529–556
3. Hanna SR (1981) Lagrangian and Eulerian time-scale in the daytime boundary layer. J Appl Meteorol 20:242–249
4. Anfossi D, Rizza U, Mangia C, Degrazia GA, Pereira Marques Filho E (2006) Estimation of the ratio between the Lagrangian and Eulerian time scales in an atmospheric boundary layer generated by large eddy simulation. Atmos Environ 40:326–337

5. Corrsin S (1963) Estimates of the relations between Eulerian and Lagrangian scales in large Reynolds number turbulence. J Atmos Sci 20:115–119

6. Mortarini L, Ferrero E, Falabino S, Trini Castelli S, Richiardone R, Anfossi D (2013) Low-frequency processes and turbulence structure in a perturbed boundary layer. Q J R Meteorol Soc 139:1059–1072.

7. Harman IN, Böhm, JJ Finnigan, Hughes D, 2016. Spatial variability of the flow and turbulence within a model canopy. Bound-Layer Meteorol 160:357–396

8. Poggi D, Katul GG, Cassiani M (2008) On the anomalous behavior of the Lagrangian structure function similarity constant inside dense canopies. Atmos Environ 42:4212–4231

9. Haverd V, Leuning R, Griffith D, van Gorsel E, Cuntz M (2009) The Turbulent Lagrangian Time Scale in Forest Canopies Constrained by Fluxes, Concentrations and Source Distributions. Boundary-Layer Meteorol 130:209–228

10. Dallman A, Di Sabatino S, Fernando HJS (2013) Flow and turbulence in an industrial/suburban roughness canopy. Environ Fluid Mech 13:279–307

11. Castro IP, Cheng H, Reynolds R (2006) Turbulence over urban-type roughness: deductions from wind-tunnel measurements. Bound-Layer Meteorol 118:109–131

12. Raupach MR (1989) Applying Lagrangian fluid mechanics to infer scalar source distributions from concentration profiles in plant canopies. Agric For Meteorol 47:85–108

13. Taylor GI (1921) Diffusion by continuous movements. Proc Lond Math Soc 20:196

14. Rotach MW (1999) On the influence of the urban roughness sublayer on turbulence and dispersion. Atmos Environ 33:4001–4008

15. Roth M, Inagaki A, Sugawara H, Kanda M (2015) Small-scale spatial variability of turbulence statistics, (co)spectra and turbulent kinetic energy measured over a regular array of cube roughness. Environ Fluid Mech 15:329–348

16. Nosek S, Kukačka L, Kellnerova R, Jurčàkovà K, Jaňour Z (2016) Ventilation processes in a three-dimensional street canyon. Bound-Layer Meteorol 159:259–284

17. Buccolieri R, Vigö H, Sandberg N, Di Sabatino S (2017) Direct measurements of the drag force over aligned arrays of cubes exposed to boundary-layer flows. Environ Fluid Mech 17:373–394

18. Monnier B, Goudarzi SA, Vinuesa R, Wark C (2018) Turbulent structure of a simplified urban fluid flow studied through stereoscopic particle image velocimetry. Bound-Layer Meteorol 166:239–268

19. Tomas JM, Eisma HE, Pourquie MJBM, Elsinga GE, Jonker HJJ, Westerweel J (2017) Pollutant dispersion in boundary layers exposed to rural-to-urban transitions: Varying the spanwise length scale of the roughness. Bound-Layer Meteorol 163: 225–251

20. Castro IP, Xie Z-T, Fuka V, Robins AG, Carpentieri M, Hayden P, Hertwig D, Coceal O (2017). Measurements and computations of flow in an urban street system. Bound-Layer Meteorol 162: 207–230

21. Saeedi M, Wang B-C (2017) Large-eddy simulation of turbulent flow and structures within and above an idealized building array. Environ Fluid Mech 17:1127–1152

22. Goulart EV, Coceal O, Belcher SE (2018) Dispersion of a passive scalar within and above an urban street network. Bound-Layer Meteorol 166:351–366

23. Grimmond CSB, Oke TR (1999) Aerodynamic properties of urban areas derived from analysis of urban surface form. J Appl Meteorol 38:1261–1292

24. Coceal O, Thomas TG, Castro IP, Belcher SE (2006) Mean flow and turbulence statistics over groups of urban-like obstacles. Bound-Layer Meteorol 121:491–519
25. Takimoto H, Sato A, Barlow JF, Moriwaki R, Inagaki A, Onomura S, Kanda M (2011) Particle image velocimetry measurements of turbulent flow in outdoor and indoor urban scale models and flushing motions in urban canopy layers. Bound-Layer Meteorol 140:295–314
26. Coceal O, Goulart EV, Branford S, Thomas TG, Belcher SE (2014) Flow structure and near-field dispersion in arrays of building-like obstacles. J Wind Eng Ind Aerodyn 125:52–68
27. Belcher SE, Coceal O, Goulart EV, Rudd AC, Robins AG (2015) Process controlling atmospheric dispersion through city centers. J Fluid Mech 763:51–81
28. Huq P, Franzese P (2013) Measurements of turbulence and dispersion in three idealized urban canopies with different aspect ratios and comparisons with a Gaussian plume model. Bound-Layer Meteorol 147:103–121
29. Orlandi P, Leonardi S (2006) DNS of turbulent channel flows with two- and three-dimensional roughness. J Turbul 7. DOI: 10.1080/14685240600827526
30. Carpentieri M, Robins AG (2015) Influence of urban morphology on air flow over building arrays. J Wind Eng Ind Aerod 145:61–74
31. Salvati A, Monti P, Coch Roura H, Cecere C (2019) Climatic performance of urban textures: analysis tools for a Mediterranean urban context. Ener Build 185:162–179
32. Di Bernardino A, Monti P, Leuzzi G, Querzoli G (2015) Water-channel study of flow and turbulence past a two-dimensional array of obstacles. Bound-Layer Meteorol 155:73–85
33. Tomasi C, Kanade T (1991) Detection and Tracking of Point. Detection and Tracking of Point Features. Carnegie Mellon University Technical Report CMU-CS-91–132
34. Cenedese A, Del Prete Z, Miozzi M, Querzoli G (2005) A laboratory investigation of the flow in the left ventricle of a human heart with prosthetic, tilting-disk valves. Exp Fluids 39:322–335
35. Lucas BD, Kanade T (1981) An iterative image registration technique with an application to stereo vision. In: Proceedings of the 1981 DARPA imaging understanding workshop, Washington, DC, April 1981, pp 121–130
36. Shi J, Tomasi C (1994) Good features to track. In: Proceedings of the IEEE conference on Computer Vision and Pattern Recognition (CVPR'94), Seattle, Washington, June 1994
37. Querzoli G (1996) A Lagrangian study of particle dispersion in the unstable boundary layer. Atmos Environ 30:282–291
38. Bendat JS, Piersol AG (2011) Random data: analysis and measurement procedures. Wiley, Hoboken
39. Monin AS, Yaglom AM (1971) Statistical Fluid Mechanics. Vol. 1 MIT Press
40. Wang QZ, Squires KD, Wu X (1995) Lagrangian statistics in turbulent channel flows. Atmos Environ 29:2417–2427
41. Guala M, Liberzon A, Tsinober A, Kinzelbach W (2007) An experimental investigation on Lagrangian correlations of small-scale turbulence at low Reynolds number. J Fluid Mech 574:405–427
42. Cheng H, Castro IP (2002) Near wall flow over urban-like roughness. Bound-Layer Meteorol 104:229–259
43. Finnigan J (2000) Turbulence in plant canopies. Annu Rev Fluid Mech 32:519–571
44. Salizzoni P, Marro M, Soulhac L, Grosjean N, Perkins RJ (2011) Turbulent transfer between street canyons and the overlying atmospheric boundary layer. Bound-Layer Meteorol 141:393–414
45. Pelliccioni A, Monti P, Leuzzi G (2016). Wind-speed profile and roughness sublayer depth modelling in urban boundary layers. Bound-Layer Meteorol 160:225–248

46. Snyder WH (1972) Similarity Criteria for the Application of Fluid Models to the Study of Air Pollution Meteorology. Bound-Layer Meteorol 3:113–134

47. Uehara K, Wakamatsu S, Ooka R (2003) Studies on critical Reynolds number indices for wind-tunnel experiments on flow within urban areas. Bound-Layer Meteorol 107:353–370

48. Leonardi S, Castro IP (2010) Channel flow over large cube roughness: a direct numerical simulation study. J Fluid Mech 651:519–539

49. Jimenez J (2004) Turbulent flows over rough walls. Annu Rev Fluid Mech 36:173-196

50. Leonardi S, Orlandi P, Djenidi L, Antonia RA (2004) Structure of turbulent channel flow with square bars on one wall. Int. J Heat Fluid Flow 25:384–392

51. Leonardi S, Orlandi P, Antonia RA (2007) Properties of d- and k-type roughness in a turbulent channel flow. Physics of Fluids 19:125101

52. Pasquill F (1974) Atmospheric diffusion, Wiley, New York, 429pp

53. Michioka T, Sato A, Takimoto H, Kanda M (2011) Large-Eddy simulation for the mechanism of pollutant removal from a two-dimensional street canyon. Bound-Layer Meteorol 138:195–213

54. Badas MG, Querzoli G (2011) Spatial structures and scaling in the convective bound layer. Exp Fluids 50:1093–1107

55. Reynolds RT, Castro IP (2008) Measurements in an urban-type boundary layer. Exp Fluids 45:141–156

56. Badas MG, Ferrari S, Garau M, Querzoli G (2017) On the effect of gable roof on natural ventilation in two-dimensional urban canyons. J Wind Eng Ind Aerod 162:24–34

57. Ferrari S, Badas MG, Garau M, et al (2017) The air quality in narrow two-dimensional urban canyons with pitched and flat roof buildings. Int J Environ Pollut 62:347–368

58. Garau M, Badas MG, Ferrari S, et al (2018) Turbulence and air exchange in a two-dimensional urban street canyon between gable roof buildings. Bound-Layer Meteorol 167:123–143

59. Di Bernardino A, Monti P, Leuzzi G, Querzoli G (2018). Pollutant fluxes in two-dimensional urban canopies. Urban Climate 24:80–93

60. Leuning R, Denmead OT, Miyata A, Kim J (2000) Source/sink distributions of heat, water vapour, carbon dioxide and methane in a rice canopy estimated using Lagrangian dispersion analysis. Agric For Meteorol 104:233–249

61. Brunet Y, Finnigan JJ, Raupach MR (1994) A wind tunnel study of air flow in waving wheat: single-point velocity statistics. Bound-Layer Meteorol 70:95–132

62. Kanda M, Inagaki A, Miyamoto T, Gryschka M, Raasch S (2013) A new aerodynamic parametrization for real urban surfaces. Bound-Layer Meteorol 148:357–377

63. Koeltzsch K (1999) On the relationship between the Lagrangian and Eulerian time scale. Atmos Environ 33:117–128

64. Foken T (2008) Micrometeorology. Springer

FIGURES

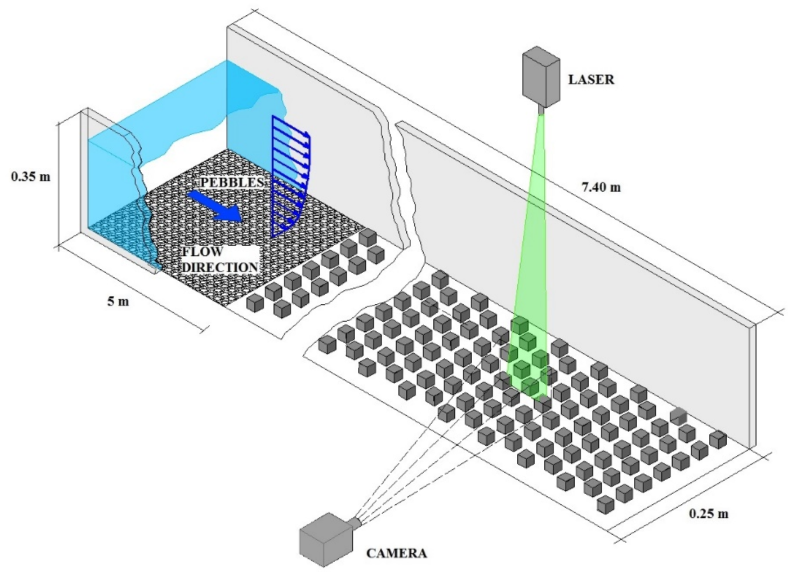

Fig. 1 Sketch, not to scale, of the experimental apparatus for the Eulerian measurements (case $\lambda_p = 0.25$)

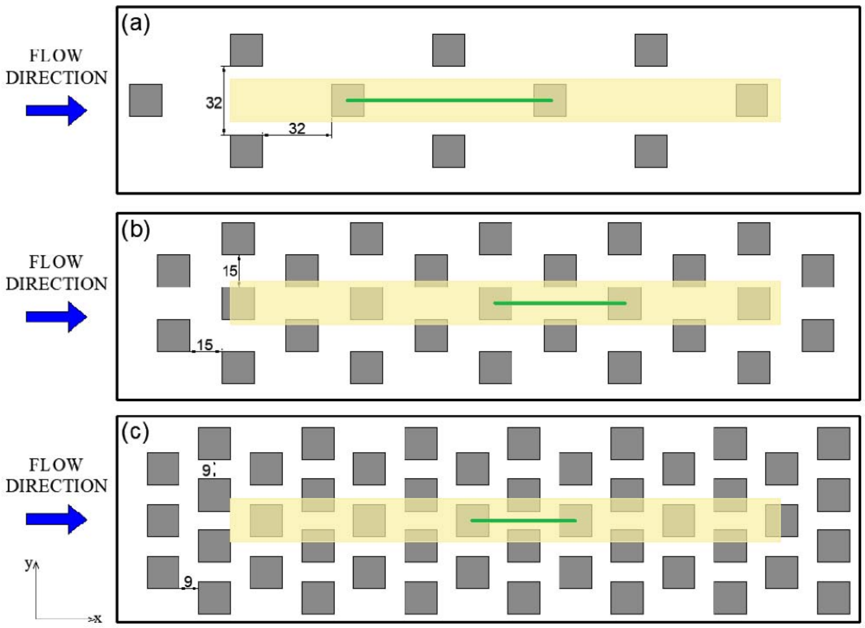

Fig. 2 Schematic plan view of the cube arrays for **a** $\lambda_p = 0.1$, **b** $\lambda_p = 0.25$ and **c** $\lambda_p = 0.4$. The green line is the signature along the horizontal plane of the vertical interrogation area used for the acquisition of the Eulerian variables, while the yellow area indicates that considered for the Lagrangian ones. The side of each cubical element is 15 mm. The streamwise and the spanwise directions are *x* and *y*, respectively. Measurements are in mm

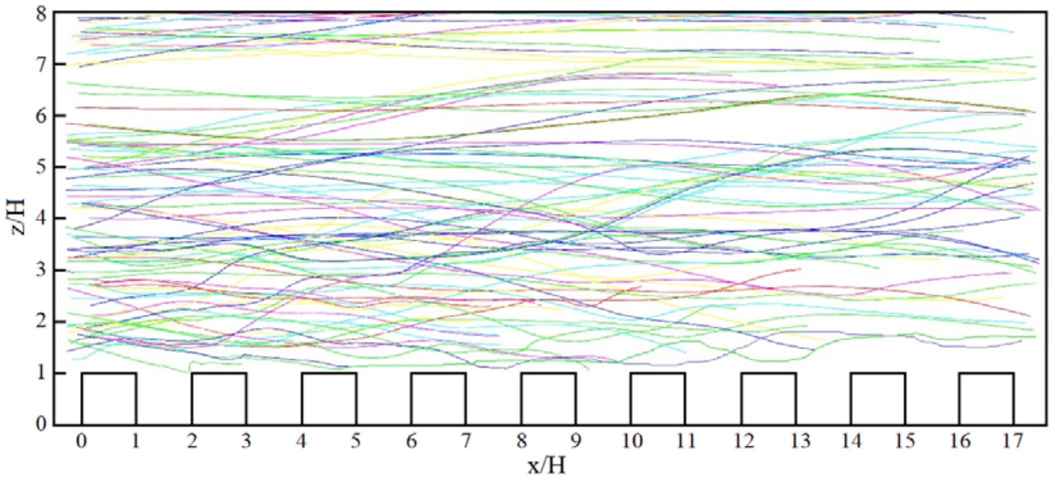

Fig. 3 Some of the particle trajectories tracked for a time longer than 350 time steps (λ_p=0.25). All the particles depicted in the figure start in a volume 1.33H wide (normal to the figure, corresponding with the depth of the light sheet coming from the halogen lamp used for the Lagrangian velocity measurement, see Fig. 2), 7H high (1<z<8, z-axis) and H/2 long (-0.5<x<0, x-axis)

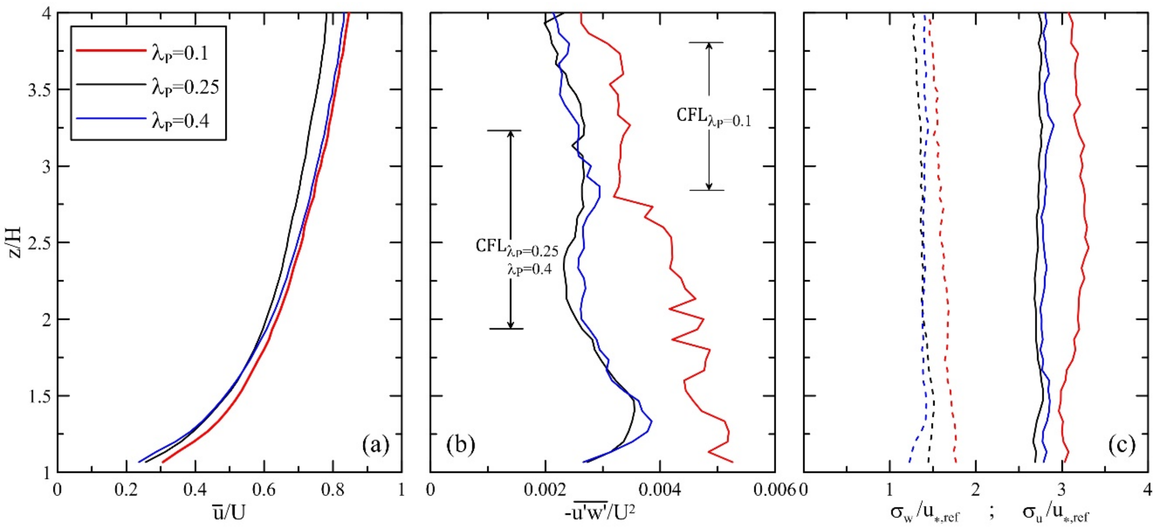

Fig. 4 Vertical profiles of normalized **a** streamwise mean velocity, **b** shear stress and **c** standard deviation of the streamwise (continuous lines) and vertical (dashed lines) velocity components for $\lambda_p = 0.1$ (red lines), $\lambda_p = 0.25$ (black) and $\lambda_p = 0.4$ (blue). The reference friction velocities calculated as the averages of the square root of the shear stresses in the CFL are $u_{*,ref}$ =0.0190 $m\ s^{-1}$, 0.0169 ms^{-1} and 0.0173 ms^{-1} for $\lambda_p = 0.1$, 0.25 and 0.4, respectively. Maximum uncertainty in the estimate of the mean velocity and the Reynolds stress is $\pm 0.6 \times 10^{-4} U$ and $\pm 0.4 \times 10^{-3} U^2$, while that of the standard deviation is $\pm 0.3\%$ (U is the free-stream velocity)

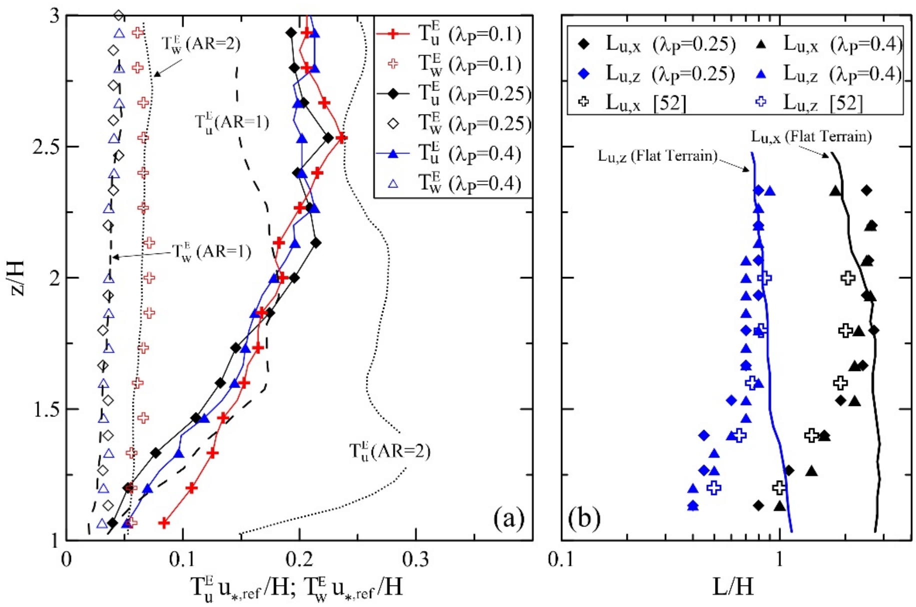

Fig. 5 a Vertical profiles of the non-dimensional Eulerian time scales of the turbulence. The vertical profiles of $T_u^E u_{*,ref}/H$ and $T_w^E u_{*,ref}/H$ found by [1] are also shown (dashed and dotted lines). **b** Vertical profiles of the non-dimensional Eulerian length scales $L_{u,x}$ (black symbols) and $L_{u,z}$ (blue symbols) for λ_p=0.25 (diamonds) and 0.4 (triangles). The open symbols refer to the results by [53] for λ_p=0.25, while the continuous lines depict $L_{u,x}/H$ (black) and $L_{u,z}/H$ (blue) estimated by [1] for flat terrain

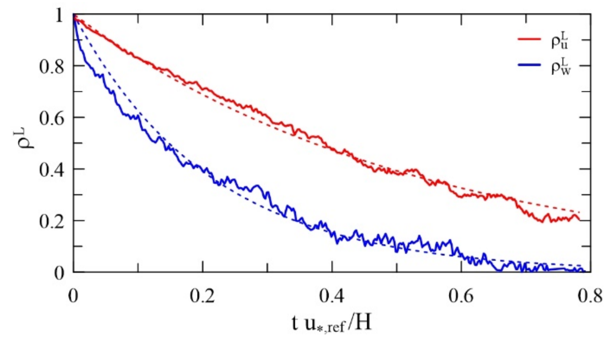

Fig. 6 Lagrangian autocorrelation functions of the streamwise (red line) and vertical (blue line) velocity components calculated at z/H=1.83 for λ_P=0.25. The dashed lines refer to the corresponding exponential fits (see text)

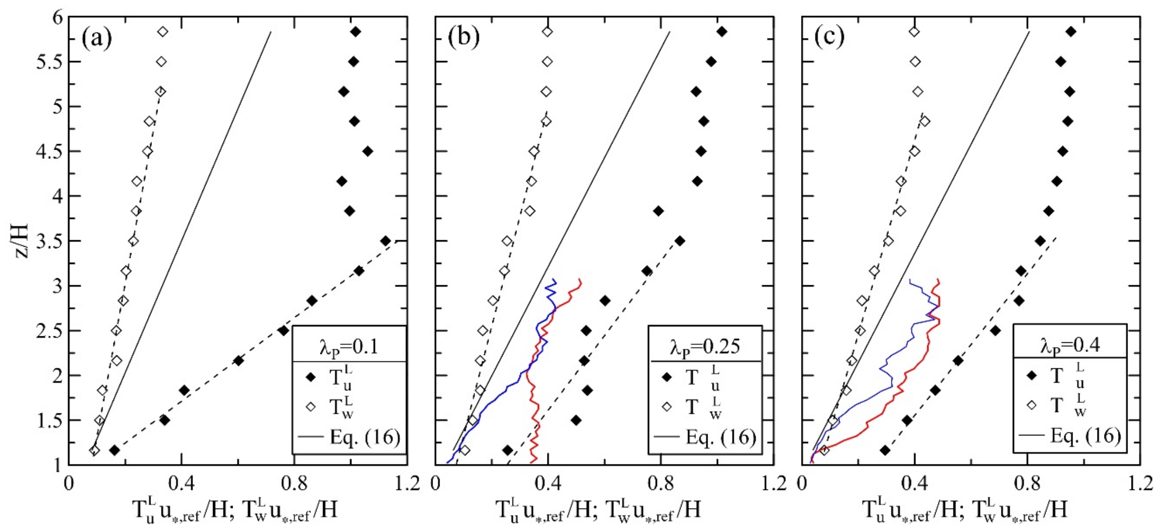

Fig. 7 Vertical profiles of the non-dimensional Lagrangian time scales estimated for **a** λ_P=0.1, **b** λ_P=0.25 and **c** λ_P=0.4. The continuous lines refer to $T^L_w u_{*,\mathrm{ref}}/H$ calculated using Eq. (16) with (*z*-*d*) instead of *z*, where *d* is the displacement height. The red and blue lines indicate $T^L_u u_{*,\mathrm{ref}}/H$ and $T^L_w u_{*,\mathrm{ref}}/H$ for the 2D cases [1], respectively. The dashed lines depict linear fits of $T^L_u u_{*,\mathrm{ref}}/H$ and $T^L_w u_{*,\mathrm{ref}}/H$ (see text)

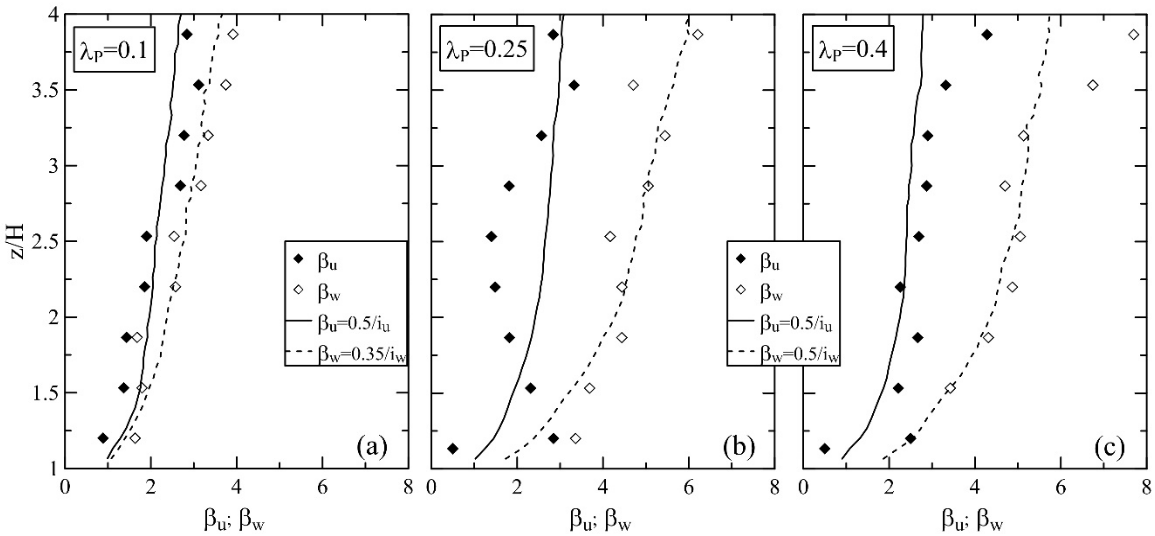

Fig. 8 Vertical profiles of $\beta_u = T_u^L/T_u^E$ and $\beta_w = T_w^L/T_w^E$ for **a** λ_P=0.1, **b** λ_P=0.25 and **c** λ_P=0.4. The continuous and dashed lines show $\beta = \gamma/i$ for the streamwise and the vertical direction, respectively

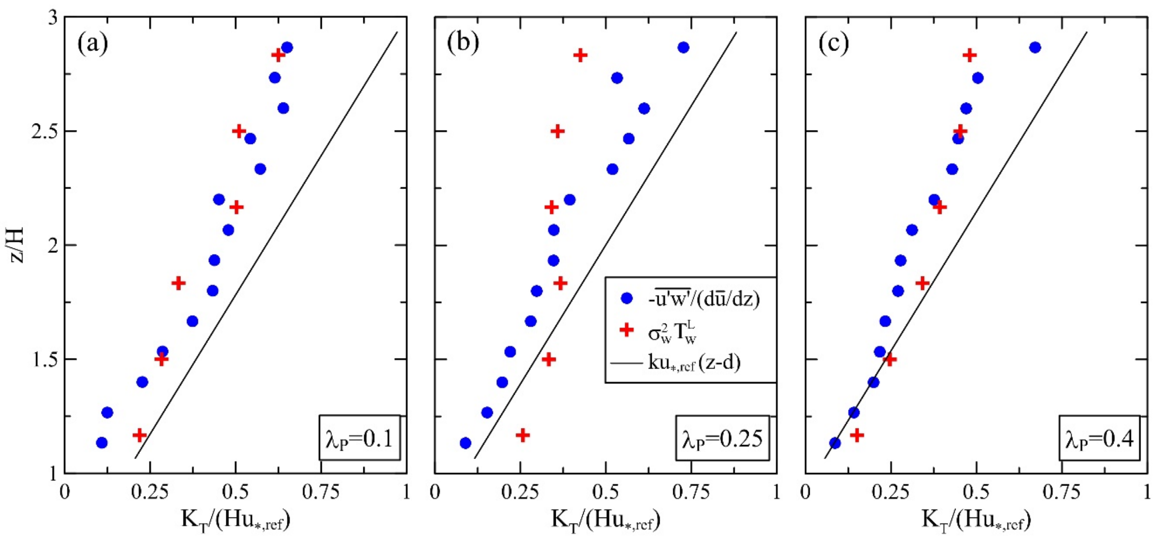

Fig. 9 Vertical profiles of the normalized turbulent diffusivity for **a** λ_P=0.1, **b** λ_P=0.25 and **c** λ_P=0.4. The values of the displacement height used in Prandtl's law are reported in Sec. 3.3